# Quantum Plasmonics: Optical Properties and Tunability of Metallic Nanorods

Jorge Zuloaga,[†,‡] Emil Prodan,[§] and Peter Nordlander[†,‡,*]

[†]Laboratory for Nanophotonics and [‡]Department of Physics and Astronomy, M.S. 61, Rice University, Houston, Texas 77005-1892 and [§]Department of Physics, Yeshiva University, New York, New York 10016

**ABSTRACT** The plasmon resonances in metallic nanorods are investigated using fully quantum mechanical time-dependent density functional theory. The computed optical absorption curves display well-defined longitudinal and transverse plasmon resonances whose energies depend on the aspect ratio of the rods, in excellent agreement with classical electromagnetic modeling. The field enhancements obtained from the quantum mechanical calculations, however, differ significantly from classical predictions for distances shorter than 0.5 nm from the nanoparticle surfaces. These deviations can be understood as arising from the nonlocal screening properties of the conduction electrons at the nanoparticle surface.

**KEYWORDS:** plasmonics · nanorod · SERS

The fascinating optical properties of nanostructured metals have captured the interest of scientists for years, driving research in a variety of fields.[1−3] The relationship among the geometry, structure, and composition of nanoparticles and their optical properties is at the forefront of research in plasmonics.[4−7] One of the most pivotal discoveries in this field has been the realization that the plasmon resonances of a metallic nanoparticle can be tuned to occur at specific frequencies by modifying the geometry of the nanoparticle. This has been demonstrated experimentally for a variety of nanostructures whose plasmonic properties were nanoengineered using reproducible, controlled processes specific to each structure.

One such plasmonic nanostructure is the metallic nanoshell,[8−12] whose plasmon frequencies can be tuned by simply varying the ratio between the thickness of the shell and the overall diameter of the nanoparticle, which can be accomplished by controlled chemical synthesis. Another highly tunable nanostructure is the metallic nanorod, which can be fabricated by either template-based or seeded growth methods.[13] In contrast to the nanoshell, the nanorod is anisotropic and can be characterized by its aspect ratio $\zeta$, defined as the ratio between its length and its width. The energies of the nanorod plasmon resonances depend quite sensitively on $\zeta$,[13−17] so varying this ratio provides the tuning mechanism for this nanostructure. The ease with which these two types of nanoparticles can be synthesized with controlled geometry has made both nanoshells and nanorods highly popular substrates for applications in sensing, medicine, and spectroscopy.[1,18,19]

While the electromagnetic properties of a wide variety of nanoparticles has been investigated quite extensively using classical electromagnetic theory,[20,21] there have only been a few *ab initio* studies on this subject. In classical electromagnetic modeling, the nanoparticles are defined by their dielectric permittivity, which changes abruptly at the nanoparticle−vacuum interface. Such classical approximations neglect the spill-out of electrons outside a realistic nanoparticle surface and also do not take into account the associated gradual change of the dielectric properties at the surfaces. Recently, there has been a great deal of interest in quantum effects such as quantum size effects, electron tunneling, and electron screening on the plasmonic response of metallic nanoparticles.[22−30] In some cases quantum effects have been found to be quite significant,[31,32] suggesting that it is of crucial importance to establish the limits of validity of classical approaches in the modeling of nanoscale plasmonic structures.

The plasmonic tunability of metallic nanoshells has been investigated using first principles time-dependent density functional theory (TDDFT).[33−35] By taking full advantage of the spherical symmetry

of this particular nanostructure, these studies were able to simulate nanoshells of realistic size and showed excellent agreement with experimental optical spectra.[36] Recently, we have extended the TDDFT quantum approach to nanostructures of cylindrical symmetry,[32] and, as a first application, investigated the optical properties of metallic nanoparticle dimers (a closely spaced pair of spherical nanoparticles). We found that, for subnanometer interparticle separation, the TDDFT calculated optical spectra and plasmon-induced electric field enhancements are profoundly different than those obtained with classical calculations. These differences originate from the electron spill-out at the surface of the nanoparticle, which introduces a source of screening that is absent in a classical description. More importantly, the electron spill-out lowers the potential barrier between the nanoparticles, enhancing the electron tunneling from one nanoparticle to the other and leading to a new plasmon mode, the so-called charge transfer plasmon, characterized by an oscillatory electric current induced between the two nanoparticles.

In this paper we apply first principles TDDFT to investigate the optical properties of silver nanorods. The calculations reveal distinct longitudinal and transverse plasmon resonances with frequencies that can be tuned by varying the aspect ratio $\zeta$ of the nanorod. The $\zeta$ dependence of the energies of both the longitudinal and transverse plasmon modes are found to be in excellent agreement with the predictions of classical electromagnetic modeling, where the surfaces of the nanoparticles are assumed to be infinitely sharp. However, the plasmon-induced electric field enhancements obtained from the quantum mechanical approach are found to be much smaller than those obtained using classical theory. The major differences occur within 0.5 nm of the surface of the nanoparticle and are due to nonlocal screening introduced by the finite electron spill-out.

## RESULTS AND DISCUSSION

For nanorods smaller than approximately 100 nm,[37] the optical response is dominated by the dipolar plasmon mode, which is the regime considered in our work. The optical spectra of small nanorods are characterized by a longitudinal and two degenerate transverse dipolar plasmon resonances. From experiment as well as classical simulations,[14] the longitudinal mode is known to strongly redshift as the aspect ratio $\zeta$ of the rod increases, while the transverse mode has the opposite behavior, that is, it blueshifts with increasing $\zeta$. The longitudinal mode is also known to be more sensitive to changes in the aspect ratio than the transverse mode.

**Jellium Model.** In our quantum simulations, we model the nanorods as prolate spheroids. In this case, their geometry is uniquely defined by their aspect ratio $\zeta$ and length of their major axis $b$. Our simulations are based on a jellium description appropriate for Ag, which as-

sumes a uniformly distributed positive ionic charge throughout the volume of the nanorod of appropriate density, and an additional constant pseudopotential representing the effect of the core electrons (see eq 3). The strength of the pseudopotential has been adjusted such that the computed work function matches the value 4.5 eV appropriate for Ag. This assures that our jellium simulations give the correct electron spill-out profile. In addition, our simulation includes a background dielectric that takes into account the polarizability of the ion cores.

In each direction, the size of the jellium model is half a lattice plane spacing larger than the physical size of the particle. For Ag, the separation between close-packed lattice planes is approximately 4 bohr, which places the jellium surfaces approximately 2 bohr outside what would be the real surface of the silver nanoparticles. For the frequency range considered in this paper, such jellium models are known to provide good quantitative descriptions of the optical properties of small metallic nanoparticles.[36] The approximation will enable us to simulate sufficiently large structures (up to more than $2 \times 10^3$ conduction electrons), a necessary condition in order to obtain a well-developed plasmonic response.

The details of the computational approach are discussed in the methods section, so here we only delineate the major steps. We employ the linear response version of TDDFT, which allows us to compute the electron density variations when small, time-oscillating external fields are applied. The absorption cross section is computed from the imaginary part of the induced dipole corresponding to these density variations. The calculations proceed as follows. In the first step we solve the equilibrium self-consistent Kohn−Sham equations for the conduction electrons of the nanorods, using an efficient numerical algorithm that takes into account the cylindrical symmetry of the nanoparticle. From the equilibrium Kohn−Sham orbitals, we compute the independent electron response function. The induced screening charge is obtained from a random phase approximation-type integral equation (see eq 6), which is solved by iterative methods.

**Tunability.** Figure 1 shows the normalized TDDFT optical absorption cross sections as a function of photon energy for nanorods of different aspect ratios $\zeta$, ranging from $\zeta = 1$ (spherical) to $\zeta = 3$ (highly elongated). In these calculations, the overall lengths $b$ of the nanorods are adjusted so that each nanorod contains exactly 510 conduction electrons. The figure shows results for longitudinal (upper panel) and transverse (lower panel) polarization of the incident light. As one can see, all absorption curves display a prominent peak which is identified as a dipolar plasmon resonance. For longitudinal polarization, we observe a strong redshift of the plasmon resonance with increasing $\zeta$. In contrast, for transverse polarization, the plasmon modes blue-
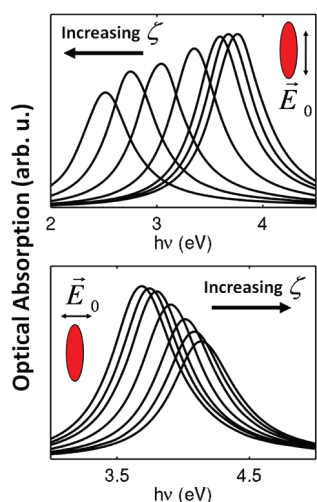
Figure 1. Optical absorption spectra calculated using TD-DFT for nanorods of different aspect ratios $\zeta$. The top panel shows the longitudinal mode for nanorods with $\zeta =$ 3, 2.5, 2, 1.5, 1.2, 1.1, and 1 with the labeling going from left to right. The bottom panel shows the transverse mode for the same $\zeta$, but with a labeling from right to left. The length $b$ of the nanorod is scaled (from $b = 48$ to 100 bohr) so that each nanorod contains the same number of electrons (510). The spectra have been normalized to the cross-sectional area of the nanorod.

shift with increasing $\zeta$, and the shifts are relatively small. The redshift of the longitudinal mode and the blue-shift of the transverse mode with increasing aspect ratio is in agreement with previous classical electromagnetic calculations and experimental data.[14] The intensity changes of the plasmon peak with increasing aspect ratio are caused by our present normalization of the spectra in the figure. The calculated spectra are all consistent with the f-sum rule,[34] (which states that the first frequency moment of the optical absorption should remain constant when the geometry of a nanoparticle is deformed), and therefore exhibit increasing peak heights with redshifting plasmon energies.

Figure 2 presents the plasmon resonant frequencies as functions of $\zeta$ as extracted from Figure 1. The two branches correspond to the longitudinal and transverse plasmon modes. For comparison, we include the
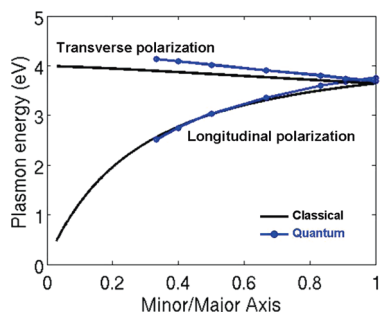


Figure 2. Longitudinal and transverse dipolar plasmon energies of a silver nanorod as a function of inverse aspect ratio $1/\zeta$ for the nanorods discussed in Figure 1. The TDDFT results are shown in blue and the classical electromagnetic results obtained using an equivalent dielectric permittivity for Ag are shown in black.
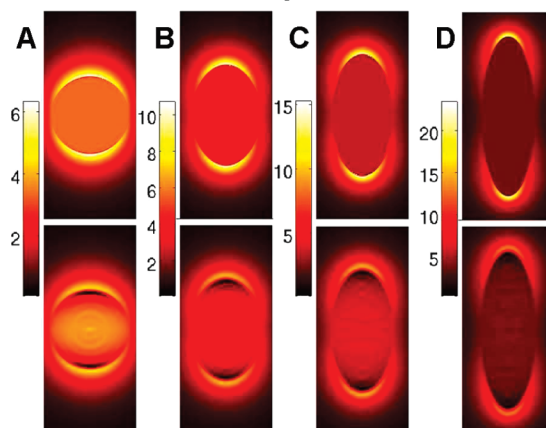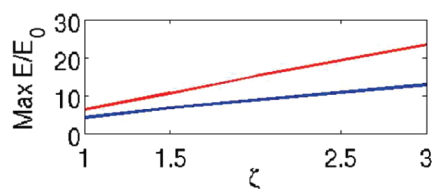


Figure 3. The upper graph shows a comparison of the maximum electromagnetic field enhancements calculated using classical electromagnetic theory (red) and TDDFT (blue) for a nanorod as a function of $\zeta$. The lower panels compare the field distributions calculated using classical electromagnetic theory (top panels) and TDDFT (bottom panels) for $\zeta = 1$ (A), $\zeta = 1.5$ (B), $\zeta = 2$ (C), and $\zeta = 3$ (D). The field enhancements were calculated for the resonant frequency of the longitudinal dipolar plasmon using a broadening of $\delta = 0.27$ eV. The overall size $b$ of each nanorod has been adjusted (from $b = 48$ to 100 bohr) so they contain 510 conduction electrons.

results of classical electromagnetic calculations using the appropriate dielectric function for Ag. As can be seen, there is good quantitative agreement between classical and quantum descriptions for both the longitudinal and transverse modes. The TDDFT results slightly overestimate the energies for the transverse modes. We believe this is a quantum size effect, which is expected to be stronger for the transverse polarization due to a more pronounced electron confinement in the transverse direction.

The quantitative agreement between quantum and classical results for the nanorod plasmon energies is consistent with previous similar studies of nanoshells[35,36] and nanosphere dimers, where for interparticle separations larger than 1 nm, appreciable electron tunneling between the two nanoparticles does not occur.[32]

**Electromagnetic Field Enhancements.** We now investigate the resonant plasmon-induced electromagnetic field enhancements of nanorods using this same approach. We are primarily interested in the longitudinal dipolar plasmon mode, the primary mode of interest in applications due to its facile tunability. The bottom panels of Figure 3 show intensity maps of $E/E_0$, where $E$ is the electric field in the presence of the nanorod and $E_0$ is the applied electric field, for four nanorods of different aspect ratios. The calculations were performed at the
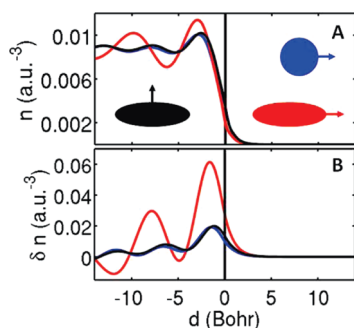
Figure 4. (A) Equilibrium electron density calculated using TDDFT as a function of distance from the particle surface along the long axis for nanorods of aspect ratios $\zeta = 1$ (blue curve) and $\zeta = 3$ (red curve), and perpendicular to the long axis for nanorods of $\zeta = 3$ (black curve). (B) Induced screening charge amplitude calculated using TDDFT as a function of distance from the particle surface along the long axis for nanorods of aspect ratios $\zeta = 1$ (blue curve) and $\zeta = 3$ (red curve), and perpendicular to the long axis for nanorods of $\zeta = 3$ (black curve). The insets show the definitions of the coordinate $d$.

corresponding resonant plasmon frequencies using both TDDFT (lowest row) and classical electromagnetism (middle row). As in Figure 1, the overall lengths $b$ of the particles were adjusted so that the total number of conduction electrons remains constant at 510. The top panel in Figure 3 shows the maximum value of the field enhancements extracted from the intensity maps as a function of $\zeta$. While for both methods of calculation the maximum intensities grow monotonically with $\zeta$, the classical calculations overestimate the growth rate. For $\zeta = 1$, for example, the maximum field enhancement calculated with classical electromagnetic theory is 6, while the TDDFT result is 4, a 33% reduction. For more elongated nanorods, the difference is even more pronounced. For $\zeta = 3$, the maximum classical field enhancement is 24, a value that is almost twice as large as the TDDFT result of 13. However, the spatial distributions of the field enhancements are similar for both the TDDFT and classical calculations.

**Nonlocal Screening.** To understand why the classical approach overestimates the field enhancements, it is helpful to analyze the electronic structure of the nanorods. Figure 4A shows the equilibrium electron density as a function of distance $d$ from the surface of the nanorod, along the long (red) and short (black) axis for a nanorod with $\zeta = 3$. For comparison, we also show the density profile for a spherical particle $\zeta = 1$ (blue). The figure reveals the expected oscillatory behavior of the electron density inside the particle due to Friedel oscillations.[36] As expected, the spill-out density is similar for all three cases, since the asymptotic electron density profile is determined by the Fermi level $\epsilon_F$ of the particle and vanishes as

$$n(d) = n_0 \exp(-\sqrt{-2\varepsilon_F}d) \qquad (1)$$

where $\epsilon_F$ is measured from the vacuum level. The electron spill-out extends to approximately 3 bohr beyond
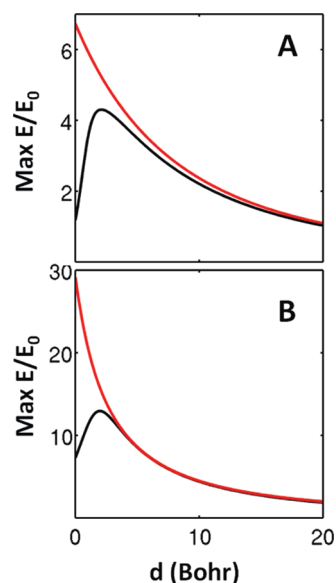


Figure 5. Electric field enhancements as a function of position $d$ around the particle surface for an aspect ratio of $\zeta = 1$ (A) and $\zeta = 3$ (B). The classical calculations are shown with red lines and the TDDFT results are shown with black lines.

the jellium surface. The main feature in Figure 4A is the pronounced anisotropy of the electron density for the elongated $\zeta = 3$ nanorod, which can be easily seen by comparing the red and black curves. This anisotropy, which becomes stronger with the increase of $\zeta$ and is due to enhanced Friedel oscillations triggered by transverse electron confinement, contributes to the diverging trend seen in Figure 3 between the quantum and classical simulations.

Figure 4B shows the amplitude of the induced screening charge density $\delta n$, at the longitudinal plasmon frequency, as a function of distance $d$ from the nanorod surface, calculated using TDDFT. The calculations were performed for the same nanorods shown in Figure 4A. The figure reveals a pronounced increase in $\delta n$ for the elongated nanorod $\zeta = 3$ along the large axis compared to the sphere $\zeta = 1$. It is this enhanced induced electron charge in the surface region that is responsible for the larger electric field enhancements seen for nanorods with larger aspect ratio. The classical electromagnetic calculations also exhibit an enhanced induced electron charge for larger $\zeta$, but in these classical calculations the induced charge is strictly an infinitely thin surface charge. The quantum calculation shows that the plasmon-induced screening charge is distributed over quite a thick region ($\sim$10 bohr) around the surface of the nanoparticle and extends out as far as the ground state spill-out shown in Figure 4A. As we shall see shortly, this quantum mechanically induced smearing of the plasmon-induced surface charge is responsible for the reduction of the electric field enhancement close to the nanoparticle surface.

We now focus on the differences seen in the plasmon-induced field enhancements between the classical and the TDDFT calculations. In Figure 5, the

local field enhancements calculated at the peak resonant frequency using TDDFT and the classical approach are compared for a spherical particle $\zeta = 1$ and for an elongated nanorod of aspect ratio $\zeta = 3$. For both particles, the classical and TDDFT field enhancements are very similar for $d$ larger than 10 bohr, but start to deviate in value when $d$ becomes smaller than 5 bohr, with the difference reaching its largest value at the particle surface ($d = 0$ bohr). For all aspect ratios investigated in Figure 1 ($1 \leq \zeta \leq 3$) the TDDFT field enhancements peak at approximately $d = 3$ bohr from the surface, while the classical field enhancements peak at the surface $d = 0$. The reason for the large discrepancy between TDDFT and classical field enhancements in the near surface region ($d < 5$ bohr) is the spatial smearing of the plasmon-induced electron density shown in Figure 4B. In the classical calculation, the induced surface charge is a delta function in $d$ and therefore results in maximal field enhancements at $d = 0$. The quantum mechanical results show that the plasmon-induced surface charge density is smeared out over quite a broad region of about 10 bohr around the surface. For $d$ outside this smeared-density region, the Coulomb potential depends only on the total induced charge density, hence the classical and TDDFT results can be expected to give similar electric field enhancements. The electric field for $d$ inside the smeared-density region is generated by only a fraction of the total induced charge density, resulting in a much weaker dependence on $d$ and reduced electric field enhancements.

**Quantum Size Effects.** The sizes of the nanorods investigated in the present paper are small ($b < 162$ bohr), so an interesting question is whether our present findings apply to realistically sized nanorods. For larger nanorods, the electronic state distribution becomes more dense and more electrons are available at the Fermi energy. This naturally leads to an increase in the electron spill-out density but does not alter the asymptotic form of the electron spill-out shown in eq 1. An increased spill-out density will make the nanorod appear larger and thus may change its effective aspect ratio and therefore its plasmon energies. Also, as discussed in Figure 5, the spill-out determines the width of the smeared plasmon-induced electron density. An increased spill-out density will introduce a further smearing of the induced electron density and may thus reduce the field enhancements even further, relative to classical results. Another size-dependent factor that may influence the plasmon energies and induced electric field distributions is the electronic density of states. In momentum space, a plasmon oscillation may be envisioned as a harmonic variation of the momentum of each conduction electron. If the energy spacings between the electronic states in the particle are too large, a plasmon oscillation is not possible. This is the reason why neither a small nanoparticle nor an individual atom exhibits a plasmonic response.
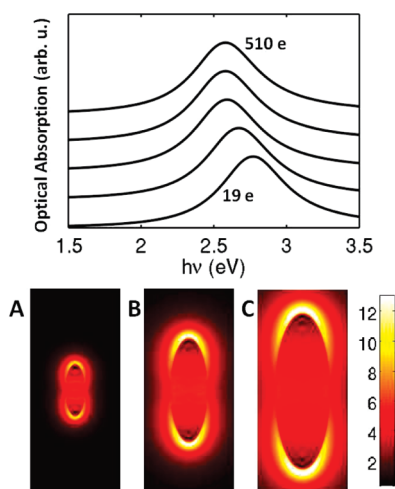


Figure 6. Top panel: Absorption spectra calculated using TDDFT for five nanorods of the same aspect ratio ($\zeta = 3$) but different major axis $b$: 34 bohr (19 electrons), 50 bohr (63 electrons), 66 bohr (151 electrons), 84 bohr (294 electrons), and 100 bohr (510 electrons) from bottom to top. The absorption spectra have been scaled so the absorption maxima are the same for each nanorod. Bottom panel: Plasmon-induced electric field enhancements for the $b = 34$ bohr (A), 66 bohr (B), and 100 bohr (C) nanorods.

In Figure 6, we compare the absorption spectra for longitudinal polarization of five nanorods with the same aspect ratio ($\zeta = 3$) but a wide array of values for the major axes $b$. In a classical description, their absorption spectra would be identical, except for a trivial scaling by a factor proportional to the number of electrons in the nanoparticle. Figure 6 clearly shows blueshifted plasmon resonances for the two smallest nanorods. For particles containing less than 100 conduction electrons, the plasmon resonance is not fully developed and quantum size effects influence the spectra, i.e., the plasmon peak positions shift with particle size. The figure shows that the plasmon resonances tend to redshift with increasing particle size. Such a redshift is similar to that observed in TDDFT calculations for nanoshells of the same aspect ratios but varying overall size and is caused by slight changes in the surface electron density distribution.[35] The spectra for the largest two particles are very similar, showing size convergence for particles containing more than 500 conduction electrons. The calculated plasmon-induced electric field distribution exhibits a similar evolution with particle size. The induced field distribution for the smallest 19-conduction-electron nanorod (Figure 6A) is not a simple dipolar distribution, but varies nonmonotonically around the surface of the tip. For the two large nanorods (Figure 6 panels B and C), the induced electric field distribution is dipolar and smooth as in Figure 3D.

**Extrapolation to Large Nanorods.** In the classical electromagnetic descriptions of small nanoparticles where retardation effects can be ignored, the optical properties are scale invariant. The magnitudes of the electromagnetic field enhancements of a nanorod are determined
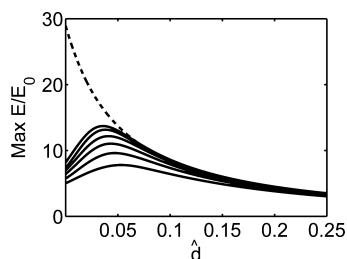
**Figure 7. Electromagnetic field enhancements as a function of $\hat{d} = d/b$ along the rod axis for rods of $\zeta = 3$. The dashed line represents the scale-invariant classical result. The solid lines show the quantum mechanical results for rods of different sizes: 19, 63, 151, 294, 882, and 2171 electrons (from bottom curve and up).**

solely by its aspect ratio $\zeta$, and the field enhancements are universal. These characteristics are only partially reproduced in the quantum calculations. Figure 7 shows the field enhancements as a function of the scaled distance from the surface of the tip, $\hat{d} = d/b$, where $d$ is the distance from the rod surface (as defined in the red inset of Figure 4), for different size nanorods with same $\zeta = 3$. The dashed line shows the scale-invariant classical enhancements, which increase monotonically with decreasing $\hat{d}$. The solid lines are the field enhancements calculated using TDDFT. The quantum mechanical effects are not scale invariant but determined by the electronic structure and the electron spill-out (eq 1). The quantum calculations differ from the classical results only at physical distances smaller than $d = d_{QM} = 0.5$ nm from the particle surface. Therefore, as the particles get larger, the quantum calculations differ from the classical results only at smaller values of $\hat{d}$. As the particle size is increased, the maximum quantum field enhancement near the surface increases monotonically, asymptotically approaching the scale-invariant electrostatic result. In real systems this limit would never be reached since retardation effects, which reduce the field enhancements, begin to play an important role when the physical dimensions of the nanorod becomes larger than a quarter of the plasmon wavelength.

Although the present calculations are performed for small model systems, the results are robust and show only small changes as the overall sizes of the structures are increased. It is clear that our prediction that the classical electromagnetic field enhancements break down near the nanoparticle surface is a real ef-

fect. The predicted distances where this breakdown happens (around 0.5 nm) are most likely underestimated. For more realistic size particles, the electron spill-out is likely to extend to larger distances, due to the closer spacings of the electronic states of the nanoparticle. In addition, and probably more importantly, our quantum approach is based on the local density approximation, and therefore neglects the electron image potential. The image potential will lower the potential barrier in the vacuum direction and will therefore increase the equilibrium electron spill-out $n$ near the surface. Since the induced charge density $\delta n$ involves excitations of electrons out of their ground state, it is likely that the image potential will have an even more significant effect on the profile of the induced charge $\delta n$ and thus on the induced electric field enhancements.

Another effect that may lead to more extended spill-out charges is the presence of sharp protrusions and edges on the particles. For such systems, the confinement from the background potential will be reduced and the electron spill-out is likely to be increased. Even the highest aspect ratio nanorods in the present study were characterized by smooth surfaces with low curvature. The effect of sharp edges and protrusions on the field enhancements near the particle surfaces will be investigated in future work.

## CONCLUSIONS

We have presented a fully quantum mechanical calculation of the electronic structure and polarizability of metallic nanorods, studying their behavior as function of nanorod aspect ratio and overall size. The calculations fully confirm the tunability of the longitudinal and transverse dipolar plasmon modes predicted using classical electromagnetic modeling. The quantum mechanically calculated field enhancements show significant differences from classical predictions at positions closer than 0.5 nm from the nanoparticle surface. These differences arise from the electronic structure of the particles and from the spatial distribution of the plasmon-induced electron surface charges. In contrast to the classical description which predicts a two-dimensional induced surface charge, the quantum description predicts a volume surface charge centered at the surface but smeared over a thickness of 0.5 nm around the surface of the particle.

## METHODS

**Quantum Calculations.** The TDDFT calculations proceeds in two steps. In the first step we compute the equilibrium electronic structure of the nanorods by solving the equilibrium self-consistent Kohn−Sham equations (the units are chosen so that $m = e = \hbar = 1$):

$$\left(-\frac{1}{2}\vec{\nabla}^2 + V_{eff}[n]\right)\psi_i = \varepsilon_i\psi_i \qquad (2)$$

where $V_{eff}[n]$ is an effective potential that depends on the electron density $n(\vec{r}) = \Sigma_{\epsilon_i < E_F}|\psi_i(\vec{r})|^2$ and contains the following terms:

$$V_{eff}[n] = V_{PS} + V_H[n - n_0] + v_{xc}[n] \qquad (3)$$

Only the s-electrons are treated explicitly in our calculations. The effect of deeper lying electrons is contained in the pseudopotential $V_{PS}$, which in our calculations is approximated by a jellium potential $V_0(\vec{r})$ that takes a finite constant value inside the particle and a zero value outside the particle. $V_H[n - n_0]$ in eq 3

is the electrostatic potential generated by the net electric charge distribution $n - n_0$, where $n_0$ is the positive ionic charge. In the present calculations, $n_0$ is approximated by a jellium distribution with a finite constant value inside the particle and zero value outside the particle. For both $V_0$ and $n_0$, the transition from the finite value to zero occurs smoothly over 1 bohr. Different termination profiles were considered for both $V_0$ and $n_0$, but were subsequently found to have little effect on the optical spectrum as long as the work functions of the particles remained the same. In addition, we have included a background dielectric medium $\epsilon_\infty$ confined to the volume of the nanoparticle, which takes into account the polarizability of the $d$ electrons. We have tuned the values of $V_0$, $n_0$, and $\epsilon_\infty$ to $-4.35$ eV, $3/4\pi r_s^3$ with $r_s = 3$ bohr, and 4.039, respectively, values that are appropriate for silver. The term $v_{xc}[n]$ is the universal exchange-correlation potential, which in the present calculations is approximated by the local density approximation (LDA) derived by Perdew and Zunger[38] by interpolating the numerical electron-gas data of Ceperley and Alder.[39]

The numerical simplifications enabled by the jellium model are significant and allow the study of nanoparticles that are sufficiently large to have a fully developed plasmon mode.[35] The optical properties of small quantum mechanical systems can be conveniently calculated using the TDDFT,[22,23,40] and its LDA approximation has been shown in many instances to provide an accurate description of the optical response for systems ranging from small atomic clusters to nanosize particles.[25,36,41]

The frequency dependent optical absorption cross section is computed from

$$\sigma_{abs} = \frac{2\pi}{c} \omega \, \text{Im}[\alpha(\omega + i\delta)] \tag{4}$$

where $\alpha(\omega)$ is the polarizability of the nanosystem when excited with a uniform, time oscillating electric field $\vec{E}_0 e^{i\omega t}$ and $\delta$ is a damping factor representing the imaginary part of the dielectric function. In the present calculations $\delta = 0.27$ eV.

The dipole–dipole polarizability $\alpha(\omega)$ is computed from the induced charge density $\delta n$ through the formula

$$\alpha(\omega) = \frac{1}{E_0} \left| \int \vec{r} \delta n(\vec{r}, \omega) \, d\vec{r} \right| \tag{5}$$

The induced charge density $\delta n$ is computed using the linear response equation:

$$\delta n(\vec{r}, \omega) = \int d\vec{r}' \chi^0(\vec{r}, \vec{r}'; \omega)[\phi(\vec{r}', \omega) + \delta v_{xc}(\vec{r}', \omega)] \tag{6}$$

where $\chi^0$ is the unscreened density–density correlation function, $\phi(\vec{r}', \omega)$ is the total electric potential when the particle is placed in the external driving potential $-\vec{r}\vec{E}_0 e^{i\omega t}$, and $\delta v_{xc}$ represents the change in the exchange-correlation potential when $n$ is replaced by $n + \delta n$.

The potential $\phi(\vec{r}, \omega)$ is calculated by solving the Poisson equation together with the following boundary condition:

$$\vec{\nabla}\varepsilon_\infty \vec{\nabla}\phi(\vec{r}, \omega) = 4\pi\delta n(\vec{r}, \omega)$$
$$\phi(\vec{r}, \omega) \rightarrow -\vec{r}\vec{E}_0 \text{ for } r \rightarrow \infty \tag{7}$$

The eqs 6 and 7 are solved self-consistently using iterative methods as previously described.[32]

The electric field enhancements are obtained from the plasmon induced electric field $\vec{E}_e(\vec{r}, \omega)$ which is the field produced by the induced screening charge $\delta n(\vec{r}, \omega)$. The maximum field enhancements occur at the plasmon resonance, $\omega = \omega_{Pl}$. The calculation of the field enhancements is performed after self-consistency of eqs 6 and 7 is obtained. The electrostatic potential from the induced charge $\phi_e(\vec{r}, \omega)$ satisfies Poisson's equation but vanishes at large separations from the particle:

$$\vec{\nabla}\varepsilon_\infty \vec{\nabla}\phi_e(\vec{r}, \omega) = 4\pi\delta n(\vec{r}, \omega)$$
$$\phi_e(\vec{r}, \omega) \rightarrow 0 \text{ for } r \rightarrow \infty \tag{8}$$

The plasmon induced field is then given by $\vec{E}_e(\vec{r}, \omega) = -\vec{\nabla}\phi_e(\vec{r}, \omega)$ and the field enhancements as $|\vec{E}_e + \vec{E}_0|/E_0$.

**Classical Calculations.** The particles studied in this work are small ($<162$ bohr) compared to the wavelength of light, so the classical calculations can be performed in the quasistatic regime. To calculate the electric field enhancements in this limit we proceed as follows: a neutral particle of dielectric constant $\epsilon(\omega)$ is placed in a static field $\vec{E}_0$. The resulting electric potential is computed by solving the Laplace's equation in all space with the appropriate boundary condition at infinity:

$$\vec{\nabla}\varepsilon\vec{\nabla}\phi(\vec{r}, \omega) = 0$$
$$\phi(\vec{r}, \omega) \rightarrow -\vec{r}\vec{E}_0 \text{ for } r \rightarrow \infty \tag{9}$$

The electric field enhancements are given by $|\vec{E}|/E_0$, where $\vec{E} = -\nabla\phi$, using $\phi$ obtained from eq 9. The optical absorption cross section in the quasistatic limit is given by

$$\sigma_{abs} = \frac{1}{2} \int d\vec{r} \frac{\omega \, \text{Im}(\varepsilon)}{4\pi} |\vec{E}|^2 \tag{10}$$

The dielectric function used for the metal in these calculations was of the Drude form:

$$\varepsilon(\omega) = \varepsilon_\infty - \frac{\omega_b^2}{\omega(\omega + i2\gamma)} \tag{11}$$

where $\epsilon_\infty$ is the background dielectric constant of the particle ($\epsilon_\infty = 4.039$ is used here for silver), $\omega_b = (4\pi n)^{1/2}$ is the bulk plasmon frequency (computed with $n = {}^3/_4\pi r_s^3$ with $r_s = 3$ bohr), and $\gamma$ represents the intrinsic damping that provides the broadening of the plasmon peak. A value of $\gamma = 0.27$ was selected to be consistent with the quantum mechanical calculations where the imaginary part is added directly to the frequency.

## REFERENCES AND NOTES

1. Lal, S.; Link, S.; Halas, N. J. Nano-optics from Sensing to Waveguiding. *Nat. Photonics* **2007**, *1*, 641–648.
2. Love, S. A.; Marquis, B. J.; Haynes, C. L. Recent Advances in Nanomaterial Plasmonics: Fundamental Studies and Applications. *Appl. Spectrosc.* **2008**, *62*, 346A–362A.
3. Hiep, H. M.; Yoshikawa, H.; Saito, M.; Tamiya, E. An Interference Localized Surface Plasmon Resonance Biosensor Based on the Photonic Structure of Au Nanoparticles and SiO$_2$/Si Multilayers. *ACS Nano* **2009**, *3*, 446–452.
4. Nehl, C. L.; Hafner, J. H. Shape-Dependent Plasmon Resonances of Gold Nanoparticles. *J. Mater. Chem.* **2008**, *18*, 2415–2419.
5. Chen, X. D.; Li, S. H.; Xue, C.; Banholzer, M. J.; Schatz, G. C.; Mirkin, C. A. Plasmonic Focusing in Rod–Sheath Heteronanostructures. *ACS Nano* **2009**, *3*, 87–92.
6. Dadosh, T.; Sperling, J.; Bryant, G. W.; Breslow, R.; Shegai, T.; Dyshel, M.; Haran, G.; Bar-Joseph, I. Plasmonic Control of the Shape of the Raman Spectrum of a Single Molecule in a Silver Nanoparticle Junction. *ACS Nano* **2009**, *3*, 1988–1994.
7. Wang, W.; Li, Z. P.; Gu, B.; Zhang, Z. Y.; Xu, H. X. Ag@SiO$_2$ Core–Shell Nanoparticles for Probing Spatial Distribution of Electromagnetic Field Enhancement *via* Surface-Enhanced Raman Scattering. *ACS Nano* **2009**, *3*, 3493–3496.
8. Oldenburg, S.; Averitt, R. D.; Westcott, S.; Halas, N. J. Nanoengineering of Optical Resonances. *Chem. Phys. Lett.* **1998**, *288*, 243–247.
9. Brinson, B. E.; Lassiter, J. B.; Levin, C. S.; Bardhan, R.; Mirin,

N.; Halas, N. J. Nanoshells Made Easy: Improving Au Layer Growth on Nanoparticle Surfaces. *Langmuir* **2008**, *24*, 14166–14171.

10. Preston, T. C.; Signorell, R. Growth and Optical Properties of Gold Nanoshells Prior to the Formation of a Continous Metallic Layer. *ACS Nano* **2009**, *3*, 3696–3706.

11. Storti, B.; Elisei, F.; Abbruzzetti, S.; Viappiani, C.; Latterini, L. One-Pot Synthesis of Gold Nanoshells with High Photon-to-Heat Conversion Efficiency. *J. Phys. Chem. C* **2009**, *113*, 7516–7521.

12. Ochsenkuhn, M. A.; Jess, P. R. T.; Stoquert, H.; Dholakia, K.; Campbell, C. J. Nanoshells for Surface-Enhanced Raman Spectroscopy in Eukaryotic Cells: Cellular Response and Sensor Development. *ACS Nano* **2009**, *3*, 3613–3621.

13. Perez-Juste, J.; Pastoria-Santos, I.; Liz-Marzan, L. M.; Mulvaney, P. Gold Nanorods: Synthesis, Characterization and Applications. *Coord. Chem. Rev.* **2005**, *249*, 1870–1901.

14. Link, S.; Mohamed, M. B.; El-Sayed, M. A. Simulation of the Optical Absorption Spectra of Gold Nanorods as a Function of Their Aspect Ratio and the Effect of the Medium Dielectric Constant. *J. Phys. Chem. B* **1999**, *103*, 3073–3077.

15. Mohammadi, A.; Sandoghdar, V.; Agio, M. Gold Nanorods and Nanospheroids for Enhancing Spontaneous Emission. *New. J. Phys.* **2008**, *10*, 105015.

16. Tzekezis, C.; Papanikolau, N.; Almpanis, E.; Stefanou, N. Tailoring Plasmons with Metallic Nanorod Arrays. *Phys. Rev. B* **2009**, *80*, 125124.

17. Chau, Y. F.; Chen, M. W.; Tsai, D. P. Three-Dimensional Analysis of Surface Plasmon Resonance Modes on a Gold Nanorod. *Appl. Opt.* **2009**, *48*, 617–622.

18. Liao, H. W.; Nehl, C. L.; Hafner, J. H. Biomedical Applications of Plasmon Resonant Metal Nanoparticles. *Nanomedicine* **2006**, *1*, 201–208.

19. Lal, S.; Clare, S. E.; Halas, N. J. Nanoshell-Enabled Photothermal Cancer-Therapy: Impending Clinical Impact. *Acc. Chem. Res.* **2008**, *41*, 1842–1851.

20. Myroshnychenko, V.; Rodrigues-Fernandez, J.; Pastoriza-Santos, I.; Funston, A. M.; Novo, C.; Mulvaney, P.; Liz-Marzan, L. M.; de Abajo, F. J. G. Modelling the Optical Response of Gold Nanoparticles. *Chem. Soc. Rev.* **2008**, *37*, 1792–1805.

21. Perassi, E. M.; Hernandez-Garrido, J. C.; Moreno, M. S.; Encina, E. R.; Coronado, E. A.; Midgley, P. A. Using Highly Accurate 3D Nanometrology To Model the Optical Properties of Highly Irregular Nanoparticles: A Powerful Tool for Rational Design of Plasmonic Devices. *Nano Lett.* **2010**, *10*, 2097–2104.

22. Yan, J.; Gao, S. W. Plasmon Resonances in Linear Atomic Chains: Free-Electron Behaviour and Anisotropic Screening of d Electrons. *Phys. Rev. B* **2008**, *78*, 235413.

23. Quijada, M.; Borisov, A. G.; Muino, R. D. Time-Dependent Density-Functional Calculation of the Energy Loss of Antiprotons Colliding with Metallic Nanoshells. *Phys. Stat. Sol. A* **2008**, *205*, 1312–1316.

24. Johnson, H. E.; Aikens, C. M. Electronic Structure and TDDFT Optical Absorption Spectra of Silver Nanorods. *J. Phys. Chem. A* **2009**, *113*, 4445–4450.

25. Aikens, C. M.; Li, S.; Schatz, G. C. From Discrete Electronic States to Plasmons: TDDFT Optical Absorption Properties of $Ag_n$ ($n$ = 10, 20, 35, 56, 84, 120) Tetrahedral Clusters. *J. Phys. Chem. C* **2008**, *112*, 11272–11279.

26. Mao, L.; Li, Z. P.; Wu, B.; Xu, H. X. Effects of Quantum Tunneling in Metal Nanogap on Surface-Enhanced Raman Scattering. *Appl. Phys. Lett.* **2010**, *94*, 243102.

27. Toparevsky, M. C.; Zhao, K.; Xiao, D.; Zhang, Z. N.; Eguiluz, A. G. Tuning the Electronic Coupling and Magnetic Moment of a Metal Nanoparticle Dimer in the Nonlinear Dielectric-Response Regime. *Nano Lett.* **2009**, *9*, 4452–4455.

28. Frey, K.; Idrobo, J. C.; Tiago, M. L.; Reboredo, F.; Ogut, S. Quasiparticle Gaps and Exciton Coulomb Energies in Si Nanoshells: First Principles Calculations. *Phys. Rev. B* **2009**, *80*, 153411.

29. Jensen, L. L.; Jensen, L. Atomistic Electrodynamics Model for Optical Properties of Silver Nanoclusters. *J. Phys. Chem. C* **2009**, *113*, 15182–15190.

30. Morton, S. M.; Jensen, L. Understanding the Molecule-Surface Chemical Coupling in SERS. *J. Am. Chem. Soc.* **2009**, *131*, 4090–4098.

31. Yan, J.; Yuan, Z.; Gao, S. W. End and Central Plasmon Resonances in Linear Atomic Chains. *Phys. Rev. Lett.* **2007**, *98*, 216602.

32. Zuloaga, J.; Prodan, E.; Nordlander, P. Quantum Description of the Plasmon Resonances of a Nanoparticle Dimer. *Nano Lett.* **2009**, *9*, 887–891.

33. Prodan, E.; Lee, A.; Nordlander, P. The Effect of a Dielectric Core and Embedding Medium on the Polarizability of Metallic Nanoshells. *Chem. Phys. Lett.* **2002**, *360*, 325–332.

34. Prodan, E.; Nordlander, P.; Halas, N. J. Effects of Dielectric Screening on the Optical Properties of Metallic Nanoshells. *Chem. Phys. Lett.* **2003**, *368*, 94–101.

35. Prodan, E.; Nordlander, P. Structural Tunability of the Plasmon Resonances in Metallic Nanoshells. *Nano Lett.* **2003**, *3*, 543–547.

36. Prodan, E.; Nordlander, P.; Halas, N. J. Electronic Structure and Optical Properties of Gold Nanoshells. *Nano Lett.* **2003**, *3*, 1411–1415.

37. Wei, H.; Reyes-Coronado, A.; Nordlander, P.; Aizpurua, J.; Xu, H. X. Multipolar Plasmon Resonances in Individual Ag Nanorice. *ACS Nano* **2010**, *4*, 2649–2654.

38. Perdew, J. P.; Zunger, A. Self-Interaction Correction to Density-Functional Approximations for Many-Electron Systems. *Phys. Rev. B* **1981**, *23*, 5048–5079.

39. Ceperley, D. M.; Alder, B. J. Ground-State of the Electron Gas by a Stochastic Method. *Phys. Rev. Lett.* **1980**, *45*, 566–569.

40. Zangwill, A.; Soven, P. Density-Functional Approach to Local-Field Effects in Finite Systems: Photoabsorption in the Rare Gases. *Phys. Rev. A* **1980**, *21*, 1561–1572.

41. Marques, M. A. L.; Castro, A.; Rubio, A. Assessment of Exchange-Correlation Functionals for the Calculation of Dynamical Properties of Small Clusters in Time-Dependent Density Functional Theory. *J. Chem. Phys.* **2001**, *115*, 3006–3014.